Lead-Related Quantum Emitters in Diamond

by

Kevin Chia-lun Chen

B.S., California Institute of Technology (2017)

Submitted to the Department of Electrical Engineering and Computer Science
in partial fulfillment of the requirements for the degree of

Masters of Science in Electrical Engineering and Computer Science

at the

MASSACHUSETTS INSTITUTE OF TECHNOLOGY

February 2019

Signature redacted

Author .....
Department of Electrical Engineering and Computer Science
January 29, 2019

Signature redacted

Certified by..... .....
Dirk Robert Englund
Associate Professor of Electrical Engineering and Computer Science
Thesis Supervisor

Signature redacted

Accepted by ....
Leslie A. Kolodziejski
Professor of Electrical Engineering and Computer Science
Chair, Department Committee on Graduate Students

Lead-Related Quantum Emitters in Diamond

by

Kevin Chia-lun Chen

Submitted to the Department of Electrical Engineering and Computer Science
on January 29, 2019, in partial fulfillment of the
requirements for the degree of
Masters of Science in Electrical Engineering and Computer Science

Abstract

This thesis reports on quantum emission from Pb-related color centers in diamond following ion implantation and high temperature vacuum annealing. First-principles calculations predict a negatively-charged Pb-vacancy center in a split-vacancy configuration, with a zero-phonon transition around 2.3 eV. Cryogenic photoluminescence measurements performed on emitters in nanofabricated pillars reveal several transitions, including a prominent doublet near 520 nm. The splitting of this doublet, 5.7 THz, exceeds that reported for other group-IV centers. These observations are consistent with the PbV center, which is expected to have the combination of narrow optical transitions and stable spin states, making it a promising system for quantum network nodes.

Thesis Supervisor: Dirk Robert Englund
Title: Associate Professor of Electrical Engineering and Computer Science

Acknowledgments

First and foremost, I would like to express my deepest gratitude towards my research adviser, Professor Dirk Englund, whose unwavering passion in science has always kept the team motivated. He gave me an opportunity to explore the field of quantum information when I was still uncertain about my graduate research direction. Since then, he has provided constant encouragement and guidance whenever I need, pushing me through difficult times with a sense of optimism that I greatly appreciate.

I would also like to thank the rest of the Quantum Photonics group, notably Noel Wan and Dr. Sara Mouradian. They selflessly sacrifice their valuable research time to teach me everything ranging from diamond fabrication to designing photonic crystal cavities to get my research started during the beginning months. Additionally, I would like to thank Dr. Matt Trusheim, Dr. Lorenzo De Santi, Chuck Choi, Michael Walsh, and Eric Bersin, for getting me acclimated to performing photoluminescence measurements, writing codes for experiments, and uncountably other things that all attribute to the realization of this thesis. I look forward to the next few years continue exploring the frontiers of science with these wonderful folks!

Above all, I cannot thank my family enough for the unfailing support I received over the years. My parents have provided me the necessary resources and love that help shape my accomplishments to date. Lastly, no words can describe my gratefulness for my girlfriend, Caitlin, who sacrificed her life on the West coast just to be alongside by me. For this, I dedicate this thesis to the woman I love.

Contents

List of Figures

Chapter 1

Introduction

1.1 Quantum Network and Diamond NV Center

The ability to communicate over long distances with security is paramount for the functioning of modern society. To this date, the way messages are encrypted is only dependent on an assumption about an eavesdropper's computational power. That is, a third party does not have the resources to crack the encoding. In fact, the working principle remains the same today. The modern RSA encryption protocols solely rely on the exponential complexity involved in factoring unusually large prime numbers. However, similar to how the enigma machine was broken by unforeseen computational power, there is no reason to believe that RSA is immune to new technologies. Indeed, the rise of a quantum computing era imposes concerns for modern communication security. Since the formulation of the Shor's algorithm in 1994, the intertwine between quantum mechanics and information science has since garnered interests in constructing the so-called quantum network. It consists of individual nodes with local memories interconnected by propagating photons, which act as flying qubits that establish entangled routing in the network [8]. If realized, this technology could provide a quantum communication medium with unbreakable security, a solution to the potential breakdown of RSA. Furthermore, it could offer applications in other disciplines, such as enable distributed quantum computing powerful enough to solve NP-hard problems, quantum simulations critical for predicting complex behaviors of biochemical molecules, and even incredibly stable sensing devices without ever the need for calibrations.

Although the potentials of a quantum network seem unbounded, a working prototype has still not been constructed to date. This is due to the difficulty to manipulate atoms coherently at a scale in which quantum mechanics dominates over classical physics. Most hardware systems do not have the two necessary characteristics: first, the ability to store information sufficiently long and second, an efficient interface with light for control and readout. One particularly promising platform is wide-bandgap semiconductor due to its excellent solid-state spin qubit candidates and scalability [9, 10]. Diamond stands out as an excellent material that hosts a myriad of defect centers. These color centers have long spin coherence times and level structures convenient for microwave control (Figure 1.1(b)). For one, the nitrogen-vacancy center (NV) has been the most explored candidate that already demonstrated second-scale spin coherence time, long distance entanglement, and coherent control for potential gate operations [11, 12, 13, 14].

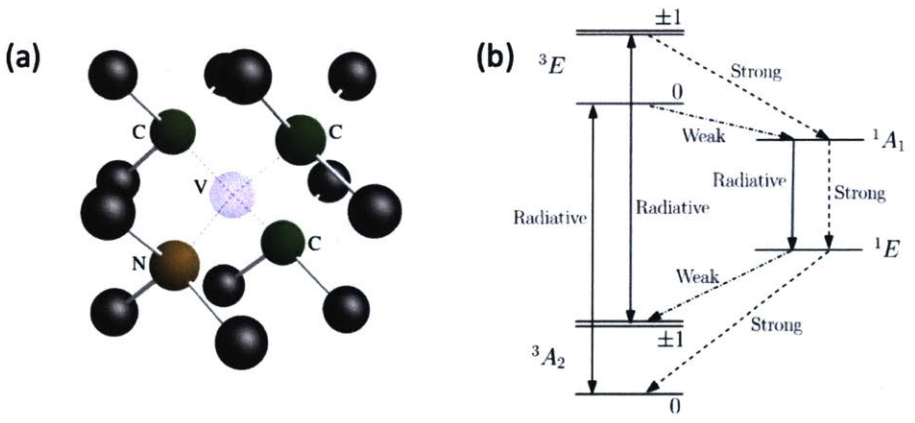

Figure 1.1: (a) Schematic of NV's trigonal pyramidal structure (C_{3v} symmetry). (b) A simplified level structure diagram of the NV optical transitions. The left hand side represents the triplet ground and excited states, which can decay to the singlet states on the right hand side via inter-system crossing. The non-cyclic pathway provides a convenient means for optical pumping. Upon applying a magnetic field, the degenerate $m = \pm 1$ states are lifted and yield two qubit states that can be manipulated by microwave pulses. Adapted from Figures 1 and 6 in Ref. [1].

However, the NV has fundamental limitations to serving as an ideal atomic memory. For one, its trigonal pyramidal structure gives rise to a first-order electric moment (Figure 1.1(a), rendering it vulnerable to nearby field fluctuations due to Stark shift. As a result, the NV optical transition shifts about the zero-phonon line (ZPL) at 637 nm, leading to an inho-

mogeneous broadening problematic for trying to encode information at a single wavelength [15, 16]. It also suffers from having much of its emission into the phonon sidebands with its low Debye-Waller factor at ~ 0.03 (Figure 1.2) [17]. These phonons dephase rapidly and cannot hold any coherent information. Therefore, there is currently still an ongoing search for a more suitable candidate as the local atomic nodes in a quantum network.

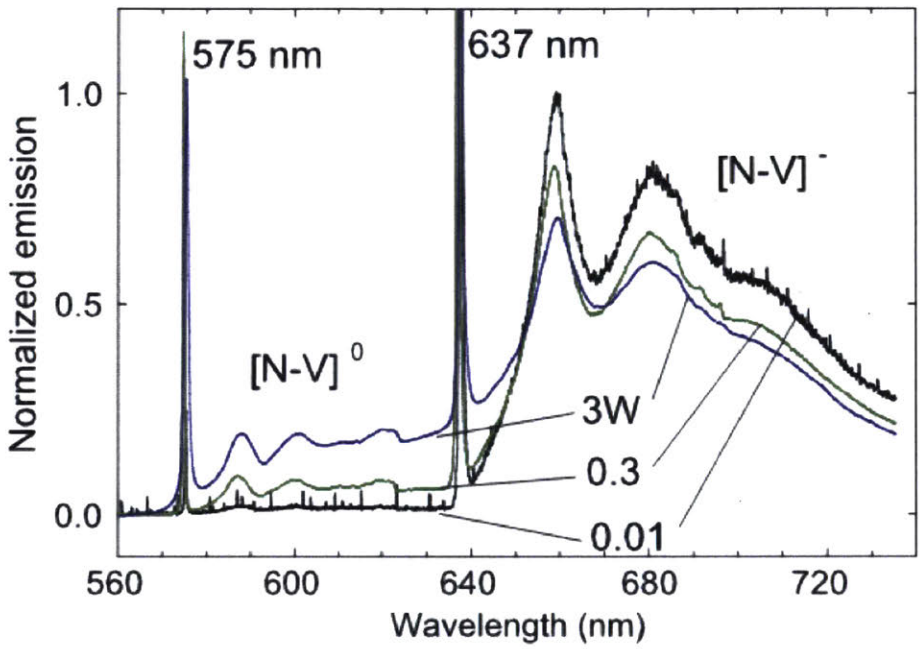

Figure 1.2: Representative spectrum of a NV in diamond. The prominent 637 nm line is the zero-phonon line, which corresponds to the optical transition between the triplet ground and excited states. The 575 nm line is the transition wavelength for the neutrally charged NV. The lower energy portion of the spectrum indicate strong phonon sidebands that make up ~97 % of the NV emission. Adapted from Figure 1 in Ref. [2].

1.2 Group-IV Quantum Emitters

More recently, novel color centers such as silicon-vacancy (SiV) centers have shown promising optical and spin properties suitable for atomic memories in a quantum network. They belong to the class of Group-IV emitters, of which those have been studied in addition to SiV are the negatively-charged germanium-vacancy (GeV) and tin-vacancy (SnV) centers [18, 19, 6, 7, 20]. In contrast to NV that is susceptible to the surrounding electric

fields, these Group-IV color centers exhibit crystallographic inversion symmetry (D_{3d}) that suppresses the first-order dipole moment and grants them resilience to environmental noises [21, 22]. As a result, the issue of spectral diffusion is much less apparent, a characteristic integral to faithfully encoding information in single-frequency photons [23, 24, 25]. In fact, only recently, Trusheim *et. al.* have observed near lifetime-limited single photons from SnV centers with linewidths down to 30 MHz [26].

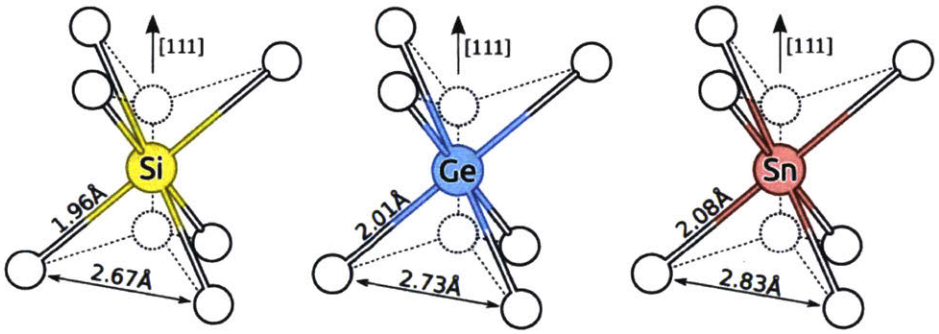

Figure 1.3: Predicted equilibrium structure for the negatively charged Group-IV diamond defect centers. The complexes exhibit inversion symmetry whose axis lies along the [111] direction. As the defect's size increases, the distances between adjacent atoms increase as well. Adapted from Figure 4 in Ref. [3].

Furthermore, the Group-IV emitters have bright optical emissions attributing to their high Debye-Waller factors, meaning their zero-phonon lines are dominant over phonon transitions. *Ab initio* density functional theory (DFT) calculations show the Huang-Rhys constants S for SiV, GeV, SnV are 0.27, 0.50, and 0.89, respectively. The corresponding Debye-Waller factors $DW = e^{-S}$ are 0.76, 0.61, and 0.41, all much higher than 0.03 for NV [27, 3].

For the remainder of this chapter, we will use SiV as an example without a loss of generality, since the rest of the Group-IV emitters are theorized to follow the same structural form. In the stable configuration, the defect rests in between a di-vacancy in the diamond lattice composed carbon atoms (Figure 1.3). The negatively-charged (we will not address neutrals or higher charged defects in this thesis) color center then has a total of eleven electrons: six from the dangling σ bonds from the carbon atoms, four from the Si atom itself, and one additional electron captured from a nearby donor. The ground and excited state configurations are presented in Figure 1.4, with the optical transition stemming from an electron relaxing from the e_g orbital to the e_u orbital [5].

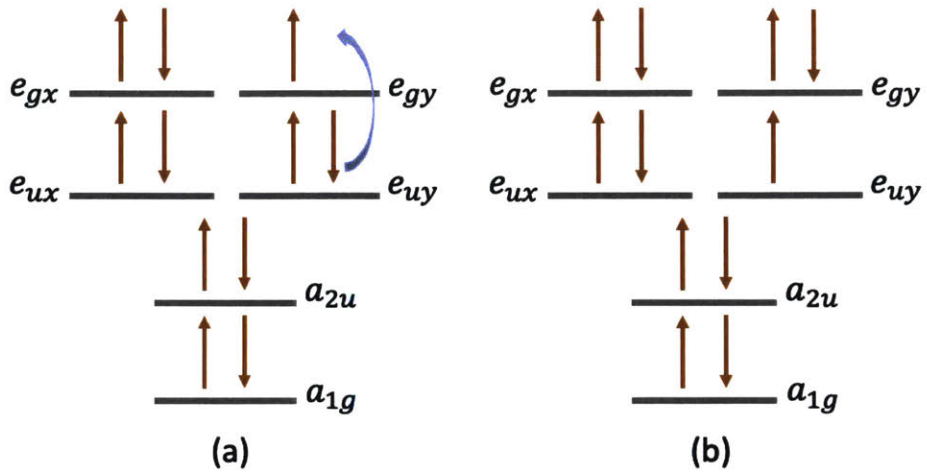

Figure 1.4: (a) The ground state configuration for SiV (and similarly for other Group-IV defect centers). There is a four-fold degeneracy since any one of the four electrons in the e_u orbitals can excite to the e_g orbitals. (b) The excited state configuration for SiV.

Notice that there exists an energy degeneracy between the e_g and e_u orbitals, which can be lifted by interactions such as spin-orbit coupling (SOC) and the dynamic Jahn-Teller (DJT) effect [3]. The former being a relativistic effect coupling spin to the electron's orbital motion under the nucleus' potential. Its Hamiltonian (with similarity transformation) is the following:

$$\mathbb{H}^{SO} = \frac{\hbar}{4mc^2}(\nabla V \times \hat{\mathbf{p}}) \cdot \frac{\hat{\mathbf{S}}}{\hbar} \approx -\frac{\lambda}{2}\hat{\mathbf{L}} \cdot \hat{\mathbf{S}} \tag{1.1}$$

where V is the electronic potential subjected to the nucleus' magnetic field, m is the electron's mass, $\hat{\mathbf{p}}$ is the electron's momentum operator, and $\hat{\mathbf{S}}$ is the spin operator consisted of Pauli matrices. In the similarity transformation form, λ represents the spin-orbit coupling strength. First, the separation between the angular and spin angular momenta indicates that the eigenstates can be written as a tensor product of the orbital and spin components. In the approximated form of the Hamiltonian, the $\hat{L}_z$ operator has off-diagonal elements that cause orbital mixing. Therefore, spin-orbit coupling transforms the orbital eigenstates $|e_x\rangle, |e_y\rangle$ to a new eigenbasis formed by $|e_+\rangle, |e_-\rangle$.

The dynamic Jahn-Teller effect also lifts the energy degeneracy, in which a spontaneous

symmetry breaking distorts the molecule to a configuration that reduces the equilibrium energy (more details regarding point symmetries can be found in Ref. [28]). Similar to spin-orbit coupling, DJT causes an orbital mixing to form the eigenbasis $|\cos\left(\frac{\phi}{2}\right) e_x \pm \sin\left(\frac{\phi}{2}\right) e_y\rangle$ that depends on a transformed normal coordinate (representing vibronic modes of the distortion) constant $\phi = \tan^{-1}\left(\frac{\Upsilon_y}{\Upsilon_x}\right)$ [29].

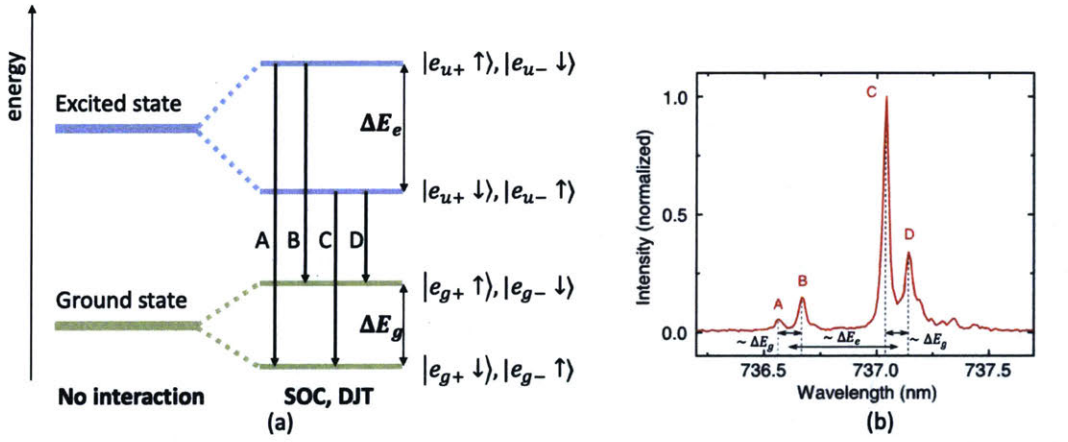

Figure 1.5: (a) Level structure for SiV. The unperturbed ground and excited states have a four-fold energy degeneracy that is lifted into doublets by spin-orbit coupling and the dynamic Jahn-Teller effect. Both interactions induce orbital mixing, render the formation of a new orbital eigenbasis consisted of $|e_+\rangle, |e_-\rangle$. (b) A representative spectrum of the SiV's fine structure level structure. The labels for the peaks correspond to the transitions in (a) appropriately. Figure (b) adapted from Figure 1(a) in Ref. [4].

Both of these effects purely affect the color center's orbital states, separating the four-fold degenerate states into doublets (Figure 1.5a). Thus, a typical fine structure spectrum of a Group-IV emitter shown in Figure 1.5b displays four lines, with the transition difference within each of the doublet being the orbital splitting modified by the dynamic Jahn-Teller effect:

$$\Delta E_{g,e} = \sqrt{\lambda_{g,e}^2 + 4\Upsilon_{g,e}^2} \tag{1.2}$$

where Υ is the quadrature sum of Υ_x and Υ_y.

In addition, due to their spin-$\frac{1}{2}$ nature, an applied magnetic field further lifts an energy degeneracy to two spin states by the Zeeman effect. The magnetic field couples to both the

orbital and spin angular momenta:

$$\mathbb{H}^Z = \mathbb{H}^{Z,L} + \mathbb{H}^{Z,S} = \gamma_L \hat{\mathbf{L}} \cdot \mathbf{B} + \gamma_S \hat{\mathbf{S}} \cdot \mathbf{B} \tag{1.3}$$

$$\approx q\gamma_L \hat{L}_z B_z + \gamma_S \hat{\mathbf{S}} \cdot \mathbf{B} \tag{1.4}$$

where $\gamma_L = \frac{\mu_B}{\hbar}$ and $\gamma_S = \frac{2\mu_B}{\hbar}$ are the orbital and electron gyromagnetic ratios, respectively.

The energy separation between the hyperfine sublevels is determined by the strength of the magnetic field along the axial [111] direction. It is important to note that any off-axis projection would induce spin mixing, therefore breaking any existent cycling transitions since spin conservation no longer applies.

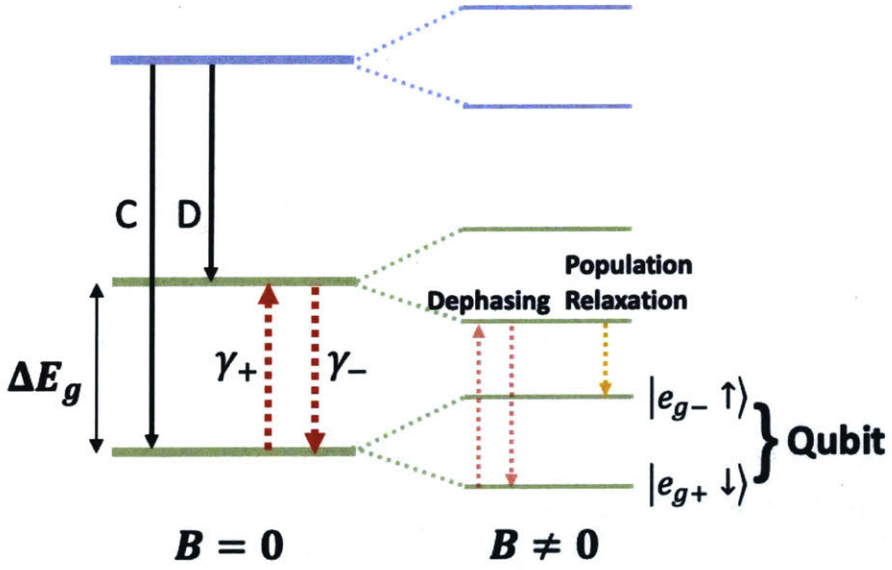

Figure 1.6: When the thermal energy kT is greater than the orbital splitting $h\Delta E_g$, there is sufficient phonon population to excite the lower ground state to the upper ground state at a transition rate γ_+. The relaxation round-trip adds either dephasing that decoheres the qubit or population relaxation that pumps the population to the upper spin sublevel $|e_{g-}\uparrow\rangle$, both destroying the qubit. This phonon scattering poses an issue to using Group-IV defect centers as atomic memories.

The two lowest energy states, $|e_{g+}, \downarrow\rangle$ and $|e_{g-}, \uparrow\rangle$, are typically chosen to form the qubit. There is, however, a fundamental source of decoherence in the level structure of these Group-IV: upward phononic transitions within the ground and excited state manifolds (Figure 1.6). However, since the qubit is encoded in the two lowest energy state, we are only concerned

with the ground state scattering processes.

γ_+ represents the rate at which thermal phonons provide sufficient energy to pump the population to the upper orbital state. As it relaxes back to the qubit sublevels, it can either return to $|g_+ \downarrow\rangle$ and accumulate an additional phase from the round trip, effectively decohering the qubit; or pump the population to the $|g_- \uparrow\rangle$ state and equivalently destroy the qubit.

The transition rates derived from Fermi's golden rule are the following [30]:

$$\gamma_+ = 2\pi\chi\rho\Delta E_g^3 n_{th}(T) \tag{1.5}$$

$$\gamma_- = 2\pi\chi\rho\Delta E_g^3 (n_{th}(T) + 1) \tag{1.6}$$

where χ, ρ are proportionality constants, ΔE_g is the ground state orbital splitting constant, and n_{th} is the phonon population governed by the Bose-Einstein distribution. They both consist of a product between the phonon density of states that scales as $\sim \Delta E_g^2$ and the electron-phonon coupling strength that scales as $\sim \Delta E_g$. Except, γ_- includes an additional term that represents spontaneous emission. Ultimately, the transition rates depend on temperature implicitly through the occupation of phononic modes n_{th}. There are two extremes worth considering: one, when the thermal energy kT is greater than the splitting energy $h\Delta E_g$, and second, when the thermal energy is much less than the orbital splitting energy. In the first case $kT > h\Delta E_g$, γ_+ is dominated by the increasing phonon density of states that is dependent on ΔE_g. On the other hand, in the second case $kT \ll h\Delta E_g$, the phonon population can be approximated by the Boltzmann distribution such that $n_{th} \approx \exp\left(-\frac{h\Delta E_g}{k_B T}\right)$. With decreasing temperature, the upward scattering rate γ_+ is exponentially suppressed, thus reducing dephasing.

Intuitively, the lower the temperature, the better the qubit's coherence time. However, for SiV, a >500 mK dilution refrigerator is required to achieve milli-second coherence time in addition to dynamical decoupling pulse sequences [31]. This experimental add-on poses undesired issues: a dilution refrigerator is difficult to acquire and to operate, and the attractiveness of solid-state spin qubits being scalable no longer applies. Therefore, it is only logical to want to increase ΔE_g rather than to decrease T in maintaining the exponential roll-

off from $\exp\left(-\frac{h\Delta E_g}{k_B T}\right)$. It has been theoretically predicted and experimentally verified that the orbital splitting increases as one goes down the Group-IV column (Figure 1.7). Hence, the temperature at which it is sufficiently low to suppress phonon occupation is higher for heavier defect centers.

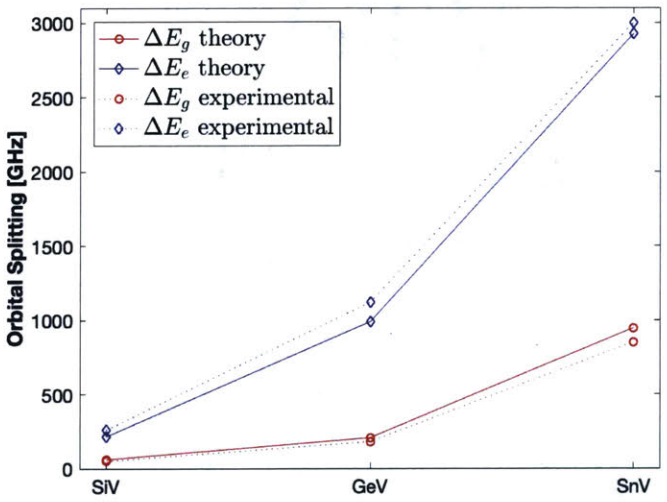

Figure 1.7: The orbital splitting as one goes down the Group-IV column in the periodic table. It is clear that the heavier the defect, the greater the splitting. It is therefore surmised that PbV would have an even greater ground state orbital splitting ΔE_g greater than 2 THz, potentially reaching a regime in which phonon transitions are frozen out at near-room temperatures. Experimental data adapted from Ref. [5], [6], [7]

It has also been shown that crystal strain distorts the defect orientation and affects the orbital states, hence acting similarly as spin-orbit coupling. Meesala *et.al.* and Maity *et.al.* demonstrated that applying longitudinal and transverse strains can effectively tune the ground and excited state orbital splitting [32, 33]. For an instance, the natural ground state splitting for SiV can be increased from 50 MHz to >600 MHz. By engineering greatly strained systems, one may avoid the need to use a dilution refrigerator to freeze out the phonon transitions. Critical to the tuning range is the strain susceptibility, which is higher for heavier defects as well. The quantum emitter of interest for this thesis, lead-vacancy (PbV) center, has not been experimentally discovered. DFT calculations predict a much higher ground state orbital splitting ($\sim$ 2 THz), translating to a long coherence time even at liquid nitrogen temperatures achievable with standard cryogenic setups [34] . Moreover, the

trend dictates that PbV would have a much greater strain susceptibility that could perhaps push towards near room-temperature operations via strain engineering [32, 33].

Chapter 2

Experiment

2.1 Sample Preparation

2.1.1 Implantation

The sample was a commercially-available type-IIa diamond ($<$ 5 ppb [N],[B]; Element6) that underwent ion implantation at an energy of 350 keV and a dose of 10^9 Pb cm^{-2} (Varian Extrion 10 - 400 keV ion implanter). Stopping range of ions in matter (SRIM) calculations (Figure 2.2a) predict that this implantation produces a Pb layer with a mean depth of (58 $\pm$ 8) nm [35]. Each implanted Pb ion is predicted to produce $\sim$2000 vacancies during implantation; although an order of magnitude more than expected for other species such as nitrogen, the predicted peak vacancy density of $\sim$ 10^{17} cm^{-3} is still well below the graphitization damage threshold for diamond [36].

Following implantation, the sample was annealed under high vacuum ($<$ 10^{-7} mbar) at 1200°C for two hours and was cleaned in a boiling tri-acid solution, consisting of hydrochloric, sulfuric and perchloric acids in 1:1:1 ratios. However, the resulting sample had a density of emitters too high to spatially isolate a single color center. Given our measurement spot size of $\sim$ 200 nm, this suggests that creation yield of Pb-related emitters (density $>$ 1 per 200 $\times$ 200 nm^2), from implanted Pb ions (10 per 1 x 1 μm^2), approaches unity.

2.1.2 Unpatterned Implant Characterization

By itself, the Pb-implanted diamond is bright without spatially separable emitters (Figure 2.1a). A representative second-order correlation measurement taken on the unpatterned, Pb-implanted diamond signifies a non-classical source of light (Figure 2.1b) [37].

$$g^{(2)}(\tau) = \frac{\langle I(t)\rangle\langle I(t+\tau)\rangle}{\langle I(t)\rangle^2} \tag{2.1}$$

A small anti-bunching dip is observed, $g^2(0) = 0.97$, indicating a very low, but non-zero, fraction of correlated single-photon emission.

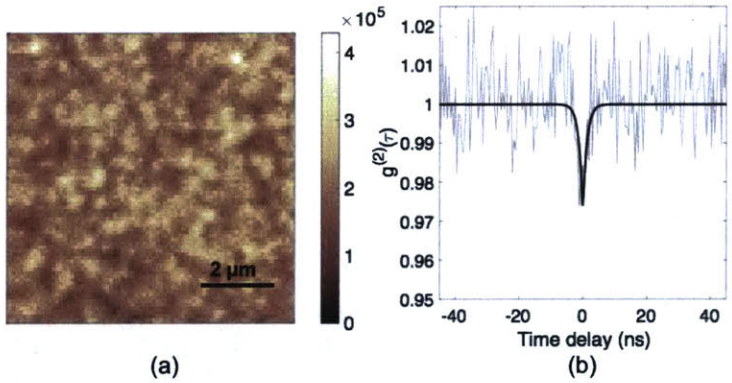

Figure 2.1: (a) Confocal scan of the unpatterned sample post-implantation. The colorbar is in counts per second. (b) A representative second-order correlation taken on an unpatterned Pb-implanted region.

2.2 Spectroscopy on Nanopillars

2.2.1 Fabrication

In order to isolate single Pb-related emitters, nanopillars were fabricated into the diamond using a combination of electron beam lithography and reactive ion etching [38, 39]. A 180 nm-thick silicon nitride (SiN) serves as our hard mask, which is deposited using plasma-enhanced chemical vapor deposition. A SiN hard mask was patterned with ZEP-520A electron beam resist and tetrafluoromethane dry etching, after which an inductively-coupled oxygen plasma

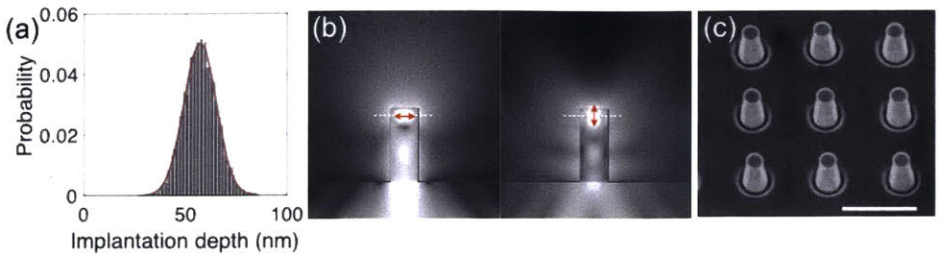

Figure 2.2: (a) Simulated Pb ion probability distribution, centered around 58 ± 8 nm in depth. (b) Field profile of an emitter in a nanopillar with a diameter of 225 nm and height of 600 nm. The red arrow represents the polarization of a dipole emitter, and the dashed white line indicates the predicted depth of Pb-related emitters. (c) Scanning electron micrograph of the fabricated nanopillar array. The scale bar is 1μ m.

RIE etched into the diamond itself. The mask was then removed using hydrofluoric acid (49%) and cleaned in a boiling tri-acid solution. Finally, the diamond was again annealed at 1200°C and cleaned using the aforementioned mixture of boiling acids.

The pillar diameters varied from 150 to 325 nm, with a height of 670 nm. For collection using an NA = 0.9 objective, finite-difference time-domain (FDTD) calculations indicate that the pillars additionally provide a 5 to 10X fluorescence collection efficiency enhancement for an emitter located at a depth of 60 nm as compared to that in an unpatterned diamond (Figure 2.2b). The scanning electron micrograph in Figure 2.2c shows the set of nanopillars with a diameter of 225 nm that were primarily investigated in this work.

2.2.2 Cryogenic Setup

Cryogenic experiments were performed using a home-built scanning confocal microscope. The samples were cooled using a closed-cycle helium cryostat (Montana Instruments) and were imaged through a 0.9 NA vacuum objective. Piezo stages (Attocube) inside the chamber allowed micrometer positioning of the sample, and galvanometer mirrors (Nutfield QS-5 OPD) enabled nanometer scanning of the confocal spot. For excitation, 532 nm light was generated by a Coherent Verdi G5 laser and 450 nm light by a laser diode. Collected fluorescence was routed to either an avalanche photodetector (Excelitas SPCM-AQRH-14) for count-rate measurements, a free-space spectrometer (Princeton Instruments, IsoPlane SCT 320) for spectral characterization, or a Hanbury Brown and Twiss interferometer consisting of

a fiber beamsplitter (Evanescent Optics) and two fiber-input APDs (Excelitas SPCM-AQRH-14-FC and Perkin Elmer SPCM-AQRH-14-FC) for second-order correlation measurements using a picosecond resolution time tagger (Pico-Quant PicoHarp 300). For measurements using the blue light, a 450 nm bandpass filter and a 500 nm shortpass filter (Thorlabs) were used on the excitation laser path, while a 500 nm longpass filter (Thorlabs) was used on the emission path. For second-order correlation measurements, a tunable shortpass filter (Semrock) was used to exclude emission from Regions III and IV (Figure 2.3). A 532 nm bandpass filter on the excitation path and 532 nm notch filter (Thorlabs) were used in experiments employing the 532 nm excitation.

2.2.3 450 nm illumination

Figure 2.3 summarizes fluorescence spectroscopy of Pb-related emitters in these nanopillars, acquired using a cryogenic confocal microscope (NA = 0.9) at a temperature of 4 K. Figure 2.3a shows a representative confocal scan of a 20 x 20 array of 225 nm diameter pillars using an excitation laser at 450 nm. Bright spots corresponding to emitters in individual nanopillars were clearly visible. A photon count rate of $\sim$ 5000 counts per second was observed at a pump power of 750 μW, which was unable to saturate the emitter due to limitations on the accessible excitation power in our setup. Figure 2.3b shows a representative spectrum from the pillar indicated by the white box in Figure 2.3a. This pillar contained a single emitter (red curve) as verified by second-order autocorrelation measurements (see inset of Figure 2.3b). After correcting for the observed sample-independent background (gray), a $g^2(0) = 0.28$ was measured, indicating quantum emission from a single emitter.

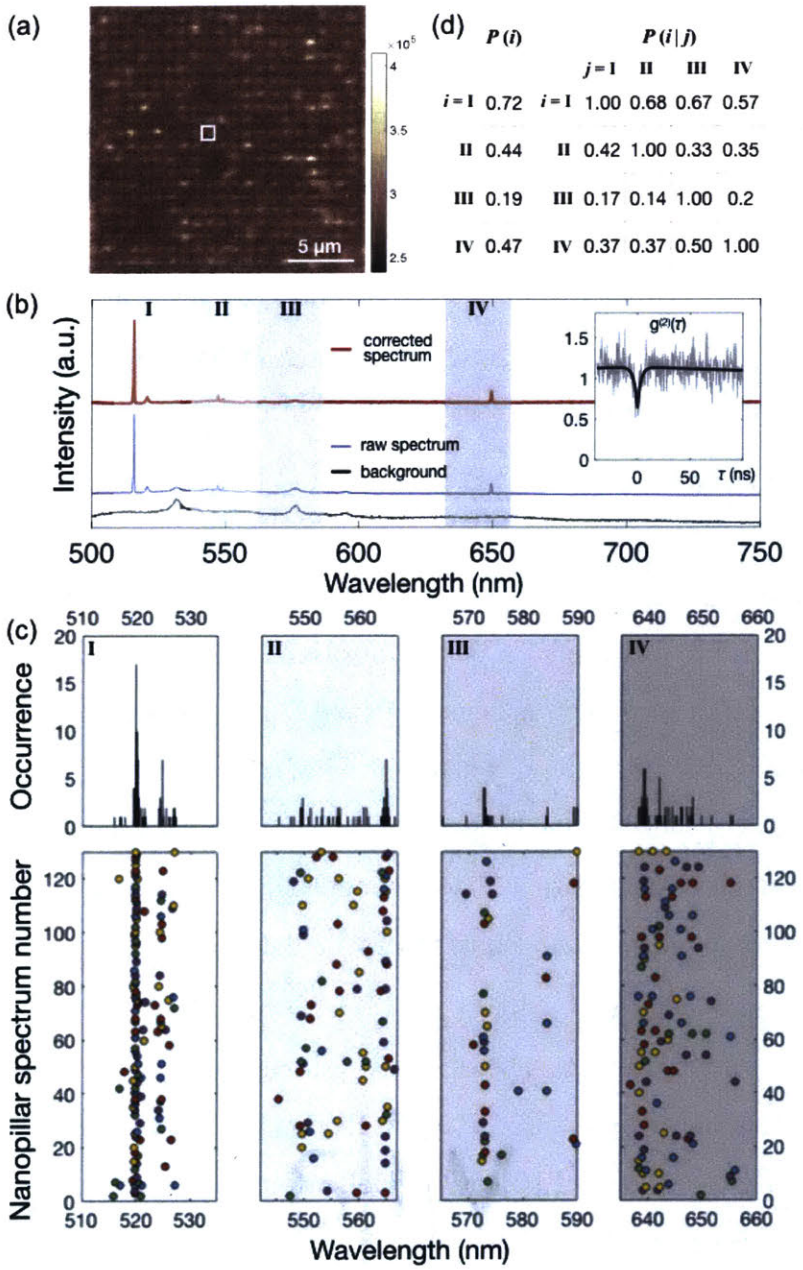

Figure 2.3: Cryogenic (4 K) emitter characterization. (a) Confocal scan of Pb-related emitters in nanopillars. Colorbar: counts per second. White box indicates a single emitter of interest as described below. (b) Emission spectrum of boxed emitter. Four regions with observed emission lines are shaded and labeled. Inset: antibunched emission with $g^2(0) = 0.52$ ($g^2(0) = 0.28$ after background correction) and antibunching time constant of 3.0 ns. (c) Summary of photoluminescence spectra from 129 pillars. Circles indicate the center of an observed emission peak, and colors correspond to individual pillars horizontally across spectral regions. Top: histogram of emission peak locations. (d) Overall and conditional probabilities for the observation of emission in each region.

Figure 2.3c shows a statistical investigation of Pb-related emitter spectral properties. Analysis of fluorescence from the 129 brightest nanopillars within the four distinct spectral regions are presented as I-IV in Figure 2.3b. The circles in Figure 2.3c indicate the fitted location of emission peaks observed for each nanopillar in the dataset. Binning the peak locations creates an inhomogeneous spectrum of Pb-related emitters (Figure 2.3c, top). Finally, the overall ($P(i)$) and conditional ($P(i|j)$) probabilities of observing an emission line in a given region were calculated (Figure 2.3d). No significant correlation between emission regions was observed with $P(i) \approx P(i|j) \forall i \neq j$.

We tentatively attribute the lines in Regions III and IV (575 and 640 nm) to neutral and negatively charged NV centers, respectively, which are formed in the implantation process from residual nitrogen atoms naturally present in the diamond [1, 2]. Many of these emitters have large shifts from the unstrained NV ZPL position, which could be due to large strains induced by Pb implantation. The presence of peaks in Region III (NV^0) and Region IV (NV^-) also indicates that the charge environment of the implanted layer is not uniform. In addition, the lack of correlation between the regions shows that the existing NVs are preferentially in a single charge state, unlike the reported photochromic NV centers in similar ultrapure type-IIa diamond without Pb implantation [40, 41].

The emission lines in Region I have not been previously reported, and we attribute them to Pb-related defect centers. The observed inhomogeneous linewidths (0.172 nm and 0.134 nm) of the prominent doublet at 520 nm in Region I are broadened between sites. However, individual diffraction-limited spots do display lines narrower than our spectrometer-limited resolution of 0.1 nm. The measured splitting of the Region I peaks, 5.2 nm (5.7 THz), is greater than that measured for the ground state of the SiV, GeV, and SnV.

The theoretically calculated and experimentally measured PbV-emitter ZPL are in relatively good agreement, with the experimentally measured ZPL doublet at 520 nm close to the simulated 517 nm [34]. Theory predicts a four-level state structure which , which points to split peaks in the emission spectra. At 4 K, we find that the ground-state splitting is 5.7 THz, which is relatively close to the theoretical predicted value of 7.25 THz. Consistent lines emerge at around 519 nm and 524 nm which we assigned to the ground state doublet (Figure 2.4b). The discrepancy, yet, between experiment and theory is likely due to the

theoretical value being too large, given that the dynamic Jahn-Teller effect was not taken into account in the calculations.

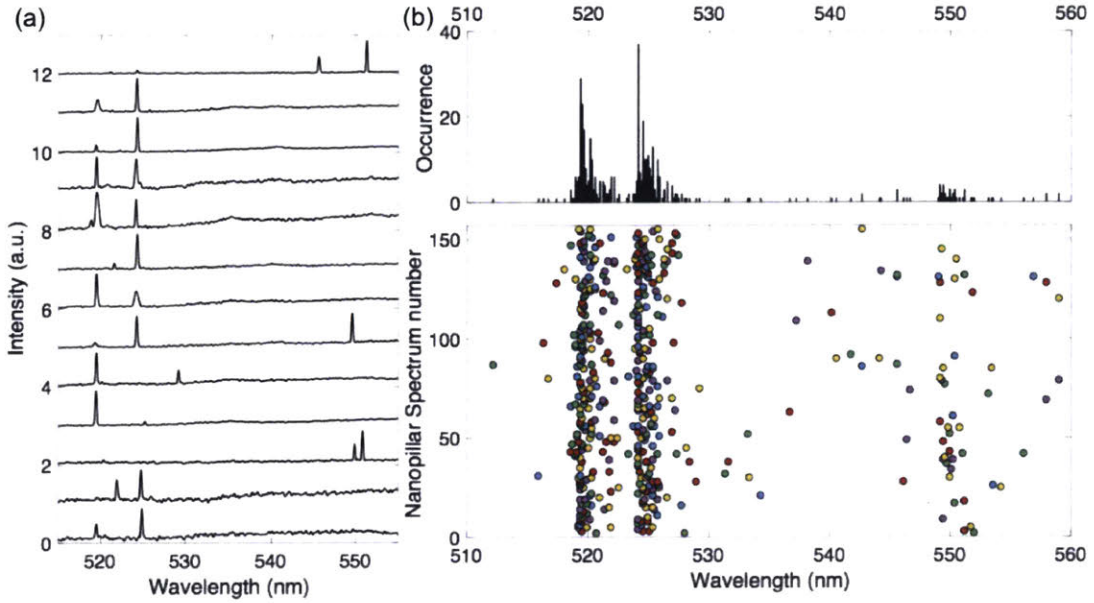

Figure 2.4: High-resolution data under 450 nm excitation. (a) Example spectra focusing only on region I which display consistent doublet near 520 nm. (b) Summary of photoluminescence spectra from 154 pillars. Circles indicate the center of an observed emission peak, and colors correspond to individual pillars horizontally across spectral regions. Top: histogram of emission peak locations.

However, emission associated with the upper excited state, which is expected to be present at higher temperatures, was not conclusively observed in experiment. These transitions could be outside of the accessible spectral range (> 500 nm) in our measurement setup. Nonetheless, the line featured at 520 nm is prominent and has yet to be reported in diamond. For this reason, we assign this peak to the PbV color center.

In addition to this pronounced line, cryogenic spectroscopy revealed other spectral features (Figure 2.5) similar to another study's report [42]. There are several possible causes for these additional lines. SnV centers produced by implantation show a broad (> 30 nm) inhomogeneous distribution following annealing at temperatures below 2000°C, including several peaks attributed to intermediate defect states. These states are eliminated upon high-pressure high-temperature annealing, which has been shown to reduce strain in the diamond lattice in addition to allowing defects to relax to lower-energy configurations. Pb implantation produces more vacancies per ion than Sn and in a smaller volume, and thus

can significantly alter the lattice during implantation. Resulting intermediate defect states and highly strained local environments could thus account for the observed emission lines. Finally, other Pb-vacancy configurations, such as a triple-vacancy or other higher-order aggregates, may be produced.

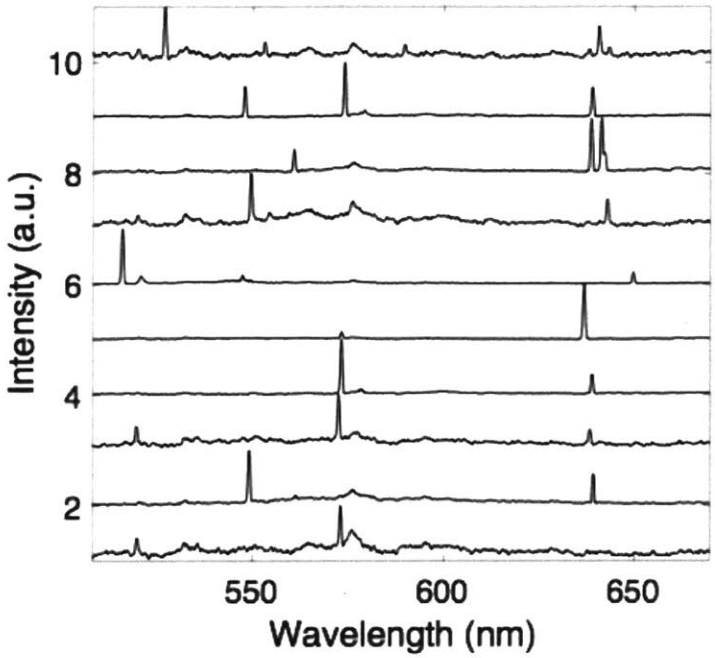

Figure 2.5: Example spectra under 450 nm excitation. Lines in regions I-IV are observed, without consistent correlation.

The charge stability of the PbV defect is another potential cause of additional spectral features. Theory predicts a charge transition level to be 2.71 eV above the valence band maximum. This suggests that photoionization could contribute to spectra by illumination into the phonon sideband under our pump at 450 nm (2.76 eV), as seen with NV and SiV centers [43, 44, 45]. The observed fluorescence instability in some centers under blue illumination (see Section 2.2.4) could indicate the presence of an alternate charge state. Additionally, other spectral features are observed in fluorescence under 532 nm illumination (see Section 2.2.5). Future measurements, such as photoluminescence excitation spectroscopy under varying electromagnetic and strain fields, will be required to fully determine the optical properties and electronic structure of the observed Pb-related emitters.

2.2.4 Photostability

Some Pb emitters show instability in their fluorescence emission over time. Figure 2.2.4 shows spectra of an emitter switching from a bright state, in which emission at 515 and 520 nm is present, and a dark state in which no emission was observed within that region. Interestingly, the emission wavelength of the line near 640/670 nm was correlated to the switching of the 520 nm line. This could imply a changing strain environment as the Pb emitter changed charge states via photoionization, similar to the SiV or NV, or as an indication that emission around 640 nm was also Pb-related. Further investigation is required to determine the mechanism of the shift in emission frequency. In addition to the bistability shown above, other Pb emitters showed photobleaching without recovery under continuous 450 nm illumination.

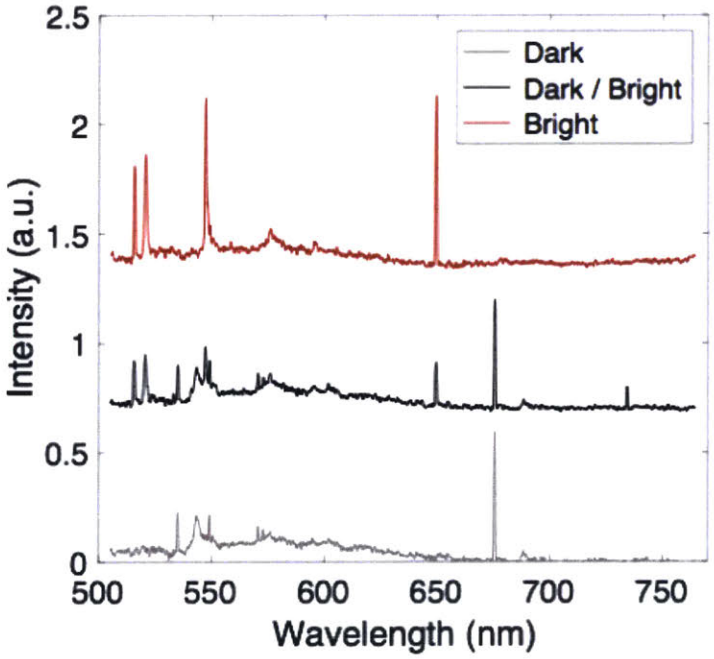

Figure 2.6: Photo-switching of a Pb-related emitter. Temporally separated spectra ($\sim$ 1 min) show distinct emission profiles.

2.2.5 532 nm illumination

The 520 nm Pb-related ZPL observed under blue excitation should not be excited under 532 nm illumination due to insufficient photon energies. However, two distinct emission lines

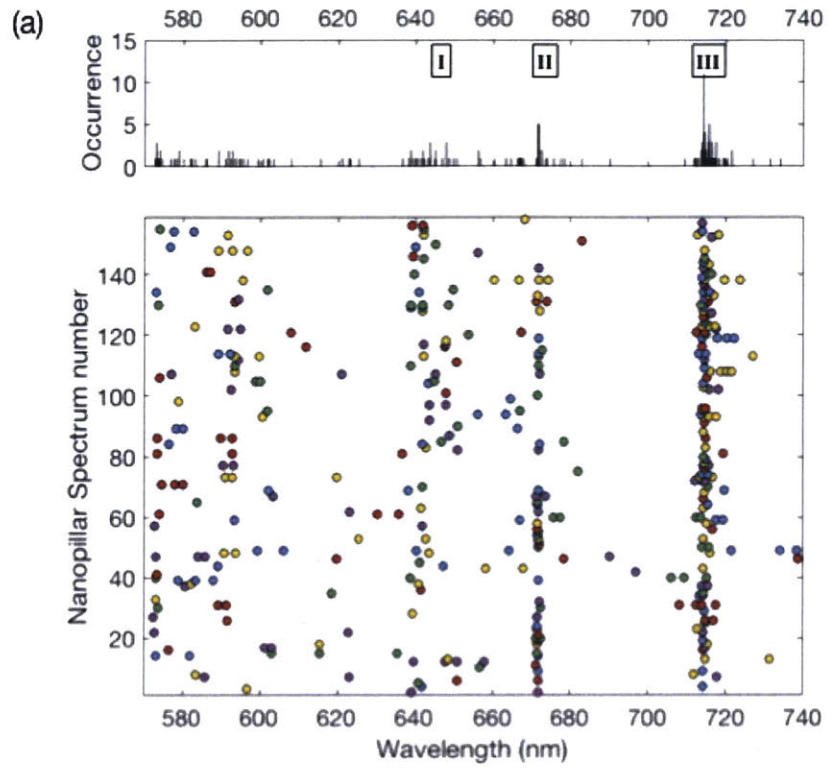

Figure 2.7: Cryogenic emission under 532 nm excitation. (a) Histogram of intensity peaks sampled over 157 pillars. Circles indicate the center of an observed emission peak, and colors correspond to individual pillars horizontally across spectral regions. (b) Comparison between conditional probabilities and individual probabilities for the observation of emission in each region. Data suggest no observable correlations

under 532 nm illumination that were not present under 450 nm emerged (Figure 2.7): 590 and 715 nm. Additionally, there existed a wide spread in emission lines from 640 to 670 nm, which we tentatively attributed to NV centers under extreme strain. As 1 GPa external stress results in an NV level shift of $\sim$ 1 THz, a 30 nm ($\sim$ 20 THz) shift implies an internal strain of 0.02, taking the Young's modulus of diamond to be $\sim$1 TPa/strain. This implies that Pb implantation significantly disrupts the diamond lattice on the nanoscale, a plausible

effect given the sheer largeness of lead atoms. A representative selection of spectra under 532 nm excitation are shown in Figure 2.9 with no noticeable correlation between emission at 590 and 715 nm.

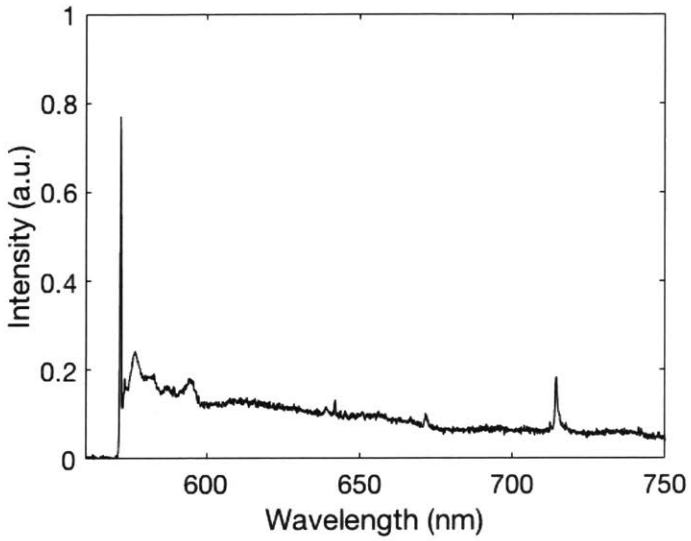

Figure 2.8: Average inhomogeneous PbV spectrum under 532 nm illumination at 4 K. Mean of emission intensity from 205 nanoposts. The 572 nm peak corresponded to the diamond Raman line.

2.2.6 Polarization and Temperature Studies

Lastly, the relative intensities of the two peaks near 520 nm at both 4 K and 40 K were compared. Figure 2.10 shows the example spectra for the two temperatures, displaying no consistent intensity ratio. Additionally, due to intensity fluctuation, the large uncertainty prevented us from conclusively claiming any temperature dependence. Tentatively, we attributed this lack of temperature dependence to a consequence of the doublet being formed by the ground state orbitals instead of the excited state orbitals. Further studies would be needed to provide more insights.

Additionally, we present the polarization dependence of the single emitter from Figure 2.3b (reproduced and color coded in Figure 2.11). Note that the emission lines of this particular emitter differed from the averaged emission from the remaining nanopillars. The polarization of the pair of lines at 515 nm (red) and 520 nm (black) were nearly orthogonal

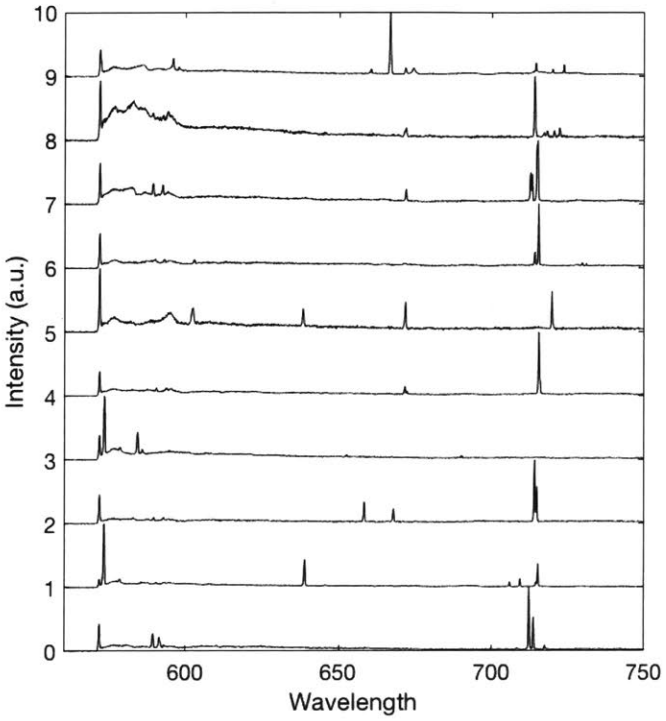

Figure 2.9: Example Pb emitter spectra under 532 nm illumination. NV-related lines are widely dispersed; peaks at 590 and 715 nm were visible, but independent.

as indicated in Figure 2.11b. All but one line (blue) in Region II (545-550 nm) appeared to be similarly polarized.

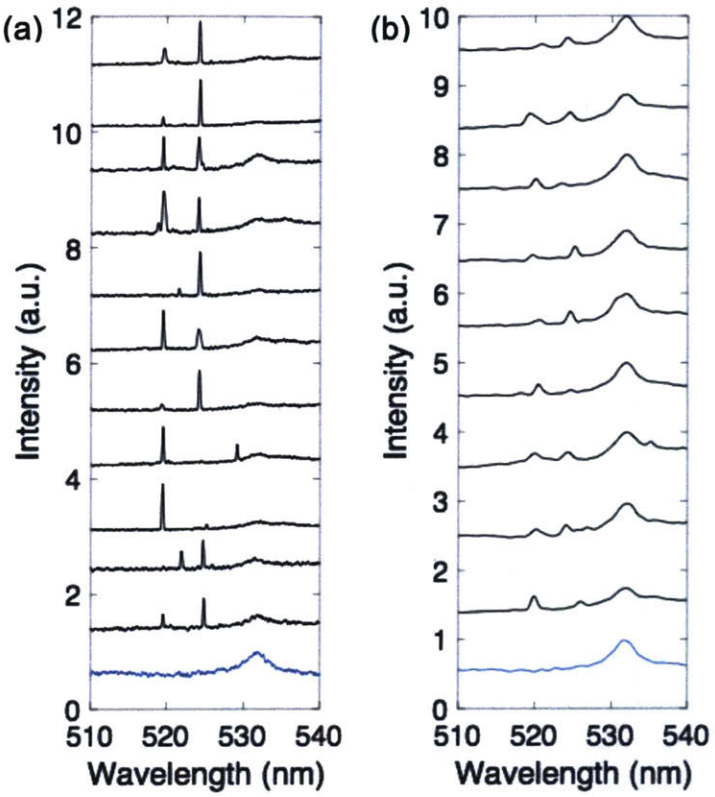

Figure 2.10: Sample spectra taken at (a) 4 K and (b) 40 K. The blue curve represents the background while the above black curves are representative spectra that display the characteristic doublet near 520 nm. The relative intensities of the two peaks at 4 K and 40 K do not systematically shift in relative intensity, suggesting the doublet stems from the split ground state orbitals rather than the excited state orbitals.

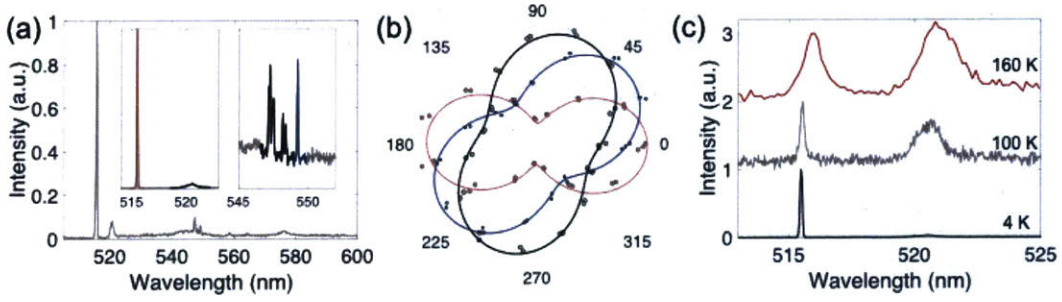

Figure 2.11: Polarization and temperature dependence. (a) Zoom-in of emission spectrum from boxed emitter in Figure 2.3a. Inset: Region I and Region II. (b). Polarization analysis of Pb spectral lines at 515 nm (red) and 520 and 547 nm (black), and 548 nm (blue).

Chapter 3

Conclusion and Outlook

This thesis presents a spectroscopic study of the quantum emission related to Pb defects in diamond. The observed anti-bunched emission near 520 nm agrees with first-principle calculations predicting a stable, negatively-charged split-vacancy PbV center. Importantly, the ground state splitting of 5.7 THz far exceeds that of other group IV-vacancy emitters (SiV, GeV, and SnV). This reaches the regime where upward phonon scattering within the ground orbital manifold is sufficiently suppressed at elevated temperatures, promising long spin coherence that is of central importance for quantum memories.

However, further experimental efforts are still very much needed. To truly affirm that the explored emitter was PbV with similar inversion symmetry as other Group-IV emitters, the excited state doublet must also be observed. These higher energy states very likely lie in the shorter wavelengths (<500 nm). Yet, due to the massive energy separation between the excited and ground states, the spontaneous emission rate could potentially be too rapid for photoluminescence excitation (PLE) measurements [26]. More novel means of detecting the excited state doublet may be required.

Additionally, the large distribution of lines suggest that the Pb-related defect center is especially susceptible to strain. High-pressure high-temperature treatment may be needed to reduce such widely inhomoegeneous distribution as seen in the case of SnV centers [7]. On the other hand, the high strain susceptibility does hint at the possibility of integrating PbV centers in nanostructures with tunable strain [32, 33, 46]. Such a degree of freedom allows for tuning to cavity resonance for cavity QED experiments or even assembling a phononic

network [47].

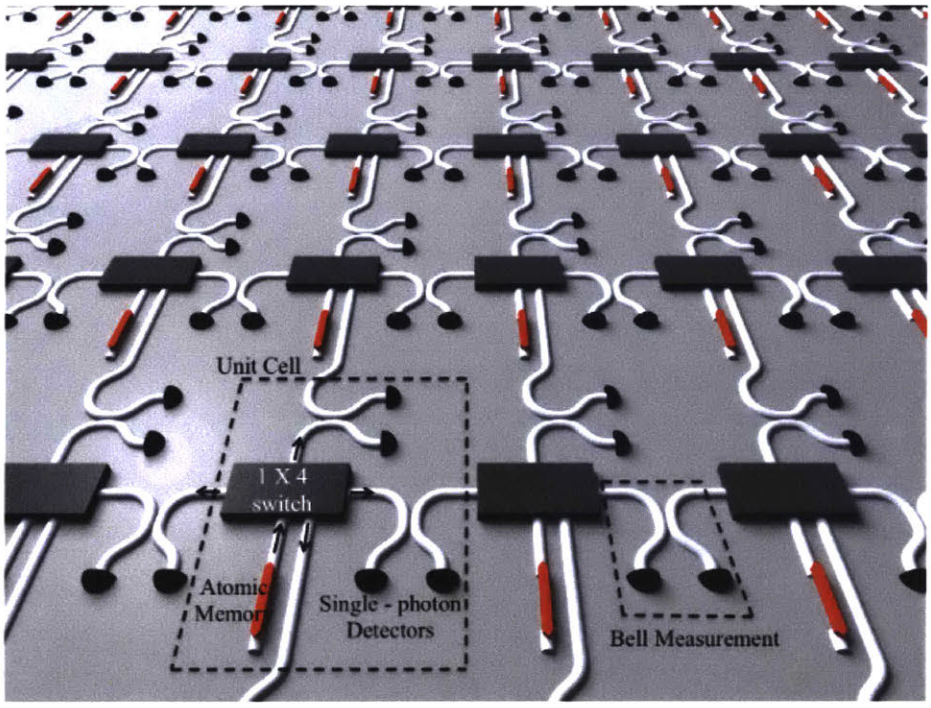

Figure 3.1: Envisioned architecture for establishing quantum routing on a nanophotonic chip. Each neighboring atomic memory node can be connected to its surrounding by measurement based entanglement. Presence of active photonic switches also allows for routing of single-photons.

Lastly, the much reduced spectral diffusion attributing to its inversion symmetry could enable PbV to locate near surfaces without being overly affected by charge states. As a result, it is perhaps a suitable candidate for coupling to photonic crystal cavities known for their high quality factors and small mode volumes. At 4 K that is readily achievable with a cryogenic setup, the PbV-cavity coupled system could demonstrate quantum optical nonlinearity and photon mediated interactions [48, 49]. Moreover, with the advancement of diamond fabrication, the PbV could even achieve strong coupling yet shown by any diamond defect center [38, 39]. Its promising spin properties granted by its large orbital splitting also renders PbV a promising candidate as an atomic memory that can be integrated to an active photonic backbone such as aluminum nitride (AlN) and lithium niobate ($LiNbO_3$) [50, 51]. Ultimately, through a combination of gas and strain tuning, the coupled emitter-cavity systems may realize a scalable nanophotonic quantum network (Figure 3.1) [52, 53].

Bibliography

[1] Marcus W. Doherty, Neil B. Manson, Paul Delaney, Fedor Jelezko, Jorg Wrachtrup, and Lloyd C.L. Hollenberg. The nitrogen-vacancy colour centre in diamond. *Physics Reports*, 2013.

[2] N.B.Manson and J.P.Harrison. Photo-ionization of the nitrogen-vacancy center in diamond. *Diamond and Related Materials*, 2005.

[3] Gergo Thiering and Adam Gali. Ab initio magneto-optical spectrum of group-iv vacancy color centers in diamond. *Physical Review X*, 2018.

[4] Tina Muller, Christian Hepp, Benjamin Pingault, Elke Neu, Stefan Gsell, Matthias Schreck, Hadwig Sternschulte, Doris Steinmuller-Nethl, Christoph Becher, and Mete Atature. Optical signatures of silicon-vacancy spins in diamond. *Nature Communications*, 2014.

[5] Christian Hepp, Tina Muller, Victor Waselowski, Jonas N. Becker, Benjamin Pingault, Hadwig Sternschulte, Doris Steinmuller-Nethl, Adam Gali, Jeronimo R. Maze, Mete Atature, and Christoph Becher. Electronic structure of the silicon vacancy color center in diamond. *Physical Review Letters*, 2014.

[6] E. A. Ekimov, S. G. Lyapin, K. N. Boldyrev, M. V. Kondrin, R. Khmelnitskiy, V. A. Gavva, T. V. Kotereva, and M. N. Popova. Germanium-vacancy color center in isotopically enriched diamonds synthesized at high pressures. *JETP Letters*, 2015.

[7] Takayuki Iwasaki, Yoshiyuki Miyamoto, Takashi Taniguchi, Petr Siyushev, Mathias H.

Metsch, Fedor Jelezko, and Mutsuko Hatano. Tin-vacancy quantum emitters in diamond. *Physical Review Letters*, 2017.

[8] H.J. Kimble. The quantum internet. *Nature*, 2008.

[9] David D. Awschalom, Lee C. Bassett, Andrew S. Dzurak, Evelyn L. Hu, and Jason R. Petta. Quantum spintronics: Engineering and manipulating atom-like spins in semiconductors. *Science*, 2013.

[10] Mete Atature, Dirk Englund, Nick Vamivakas, Sang-Yun Lee, and Joerg Wrachtrup. Material platforms for spin-based photonic quantum technologies. *Nature Materials*, 2018.

[11] M. H. Abobeih, J. Cramer, M. A. Bakker, M. Markham N. Kalb, D. J. Twitchen, and T. H. Taminiau. One-second coherence for a single electron spin coupled to a multi-qubit nuclear-spin environment. *Nature Communications*, 2018.

[12] Daniel Riedel, Immo Sollner, Brendan J. Shields, Sebastian Starosielec, Patrick Appel, Elke Neu, Patrick Maletinsky, and Richard J. Warburton. Deterministic enhancement of coherent photon generation from a nitrogen-vacancy center in ultrapure diamond. *Physical Review X*, 2017.

[13] E. Togan, Y. Chu, A. S. Trifonov, L. Jiang, J. Maze, L. Childress, M. V. G. Dutt, A. S. Sorensen, P. R. Hemmer, A. S. Zibrov, and M. D. Lukin. Quantum entanglement between an optical photon and a solid-state spin qubit. *Nature*, 2010.

[14] N. Kalb, A. A. Reiserer, P. C. Humphreys, J. J. W. Bakermans, S. J. Kamerling, N. H. Nickerson, S. C. Benjamin, D. J. Twitchen, M. Markham, and R. Hanson. Entanglement distillation between solid-state quantum network nodes. *Science*, 2017.

[15] Andrei Faraon, Charles Santori, Zhihong Huang, Victor M. Acosta, and Raymond G. Beausoleil. Coupling of nitrogen-vacancy centers to photonic crystal cavities in monocrystalline diamond. *Physical Review Letters*, 2012.

[16] Luozhou Li, Tim Schroder, Edward H. Chen, Michael Walsh, Igal Bayn, Jordan Goldstein, Ophir Gaathon, Matthew E. Trusheim, Ming Lu, Jacob Mower, Mircea Cotlet, Matthew L. Markham, Daniel J. Twitchen, and Dirk Englund. Coherent spin control of a nanocavity-enhanced qubit in diamond. *Nature Communications*, 2015.

[17] Sebastien Pezzagna, Detlef Rogalla, Dominik Wildanger, Jan Meijer, and Alexander Zaitsev. Creation and nature of optical centres in diamond for single-photon emission-overview and critical remarks. *New Journal of Physics*, 2011.

[18] Chunlang Wang, Christian Kurtsiefer, Harald Weinfurter, and Bernd Burchard. Single photon emission from siv centres in diamond produced by ion implantation. *Journal of Physics B: Atomic, Molecular and Optical Physics*, 2005.

[19] Yuri N. Palyanov, Igor N. Kupriyanov, Yuri M. Borzdov, and Nikolay V. Surovtsev. Germanium: a new catalyst for diamond synthesis and a new optically active impurity in diamond. *Scientific Reports*, 2015.

[20] S. Ditalia Tchernij, T. Herzig, J. Forneris, J. Kupper, S. Pezzagna, P. Traina, E. Moreva, I. P. Degiovanni, G. Brida, N. Skukan, M. Genovese, M. Jaksic, J. Meijer, and P. Olivero. Single-photon-emitting optical centers in diamond fabricated upon sn implantation. *ACS Photonics*, 2017.

[21] A. Sipahigil, K.D. Jahnke, L.J. Rogers, T. Teraji, J. Isoya, A.S. Zibrov, F. Jelezko, and M.D. Lukin. Indistinguishable photons from separated silicon-vacancy centers in diamond. *Physical Review Letters*, 2014.

[22] Lachlan J. Rogers, Kay D. Jahnke, Marcus W. Doherty, Andreas Dietrich, Liam P. McGuinness, Christoph Muller, Tokuyuki Teraji, Hitoshi Sumiya, Junichi Isoya, Neil B. Manson, and Fedor Jelezko. Electronic structure of the negatively charged silicon-vacancy center in diamond. *Physical Review B*, 2014.

[23] Ruffin E. Evans, Alp Sipahigil, Denis D. Sukachev, Alexander S. Zibrov, and Mikhail D. Lukin. Narrow-linewidth homogeneous optical emitters in diamond nanostructures via silicon ion implantation. *Physical Review Applied*, 2016.

[24] M.K. Bhaskar, D.D. Sukachev, A. Sipahigil, R.E. Evans, M.J. Burek, C.T. Nguyen, L.J. Rogers, P. Siyushev, M.H. Metsch, H. Park, F. Jelezko, M. Loncar, and M.D. Lukin. Quantum nonlinear optics with a germanium-vacancy color center in a nanoscale diamond waveguide. *Physical Review Letters*, 2017.

[25] Petr Siyushev, Mathias H. Metsch, Aroosa Ijaz, Jan M. Binder, Mihir K. Bhaskar, Denis D. Sukachev, Alp Sipahigil, Ruffin E. Evans, Christian T. Nguyen, Mikhail D. Lukin, Philip R. Hemmer, Yuri N. Palyanov, Igor N. Kupriyanov, Yuri M. Borzdov, Lachlan J. Rogers, and Fedor Jelezko. Optical and microwave control of germanium-vacancy center spins in diamond. *Physical Review B*, 2017.

[26] Matthew E. Trusheim, Benjamin Pingault, Noel H Wan, Mustafa Gundogan, Lorenzo De Santis, Kevin C. Chen, Michael Walsh, Joshua J. Rose, Jonas N. Becker, Benjamin Lienhard, Eric Bersin, Girish Malladi, Hassaram Bakhru, Ian Walmsley, Mete Atature, and Dirk Englund. Transform-limited photons from a tin-vacancy spin in diamond. *arXiv*, 2018.

[27] Elke Neu, Christian Hepp, Michael Hauschild, Stefan Gsell, Martin Fischer, Hadwig Sternschulte, Doris Steinmuller-Nethl, Matthias Schreck, and Christoph Becher. Low-temperature investigations of single silicon vacancy colour centres in diamond. *New Journal of Physics*, 2013.

[28] H. A. Jahn, E. Teller, and Frederick George Donnan. Stability of polyatomic molecules in degenerate electronic states - i. orbital degeneracy. *Proceedings of the Royal Society of London. Series A - Mathematical and Physical Sciences*, 1937.

[29] Christian Joachim Hepp. *Electronic Structure of the SiliconVacancy Color Center in Diamond.* PhD thesis, Saarland University, 2014.

[30] Kay D Jahnke, Alp Sipahigil, Jan M Binder, Marcus W Doherty, Mathias Metsch, Lachlan J Rogers, Neil B Manson, Mikhail D Lukin, and Fedor Jelezko. Electron-phonon processes of the silicon-vacancy centre in diamond. *New Journal of Physics*, 2015.

[31] D.D. Sukachev, A. Sipahigil, C.T. Nguyen, M.K. Bhaskar, R.E. Evans, F. Jelezko, and M.D. Lukin. Silicon-vacancy spin qubit in diamond: A quantum memory exceeding 10 ms with single-shot state readout. *Physical Review Letters*, 2017.

[32] Srujan Meesala, Young-Ik Sohn, Benjamin Pingault, Linbo Shao, Haig A. Atikian, Jeffrey Holzgrafe, Mustafa Gundogan, Camille Stavrakas, Alp Sipahigil, Cleaven Chia, Ruffin Evans, Michael J. Burek, Mian Zhang, Lue Wu, Jose L. Pacheco, John Abraham, Edward Bielejec, Mikhail D. Lukin, Mete Atature, and Marko Loncar. Strain engineering of the silicon-vacancy center in diamond. *Physical Review B*, 2018.

[33] Smarak Maity, Linbo Shao, Young-Ik Sohn, Srujan Meesala, Bartholomeus Machielse, Edward Bielejec, Matthew Markham, and Marko Loncar. Spectral alignment of single-photon emitters in diamond using strain gradient. *Physical Review Applied*, 2018.

[34] Matthew E. Trusheim, Noel H. Wan, Kevin C. Chen, Christopher J. Ciccarino, Ravishankar Sundararaman, Girish Malladi, Eric Bersin, Michael Walsh, Benjamin Lienhard, Hassaram Bakhru, Prineha Narang, and Dirk Englund. Lead-related quantum emitters in diamond. *Physical Review B*, 2018.

[35] James F.Ziegler, M.D.Ziegler, and J.P.Biersack. Srim - the stopping and range of ions in matter. In *Nuclear Instruments and Methods in Physics Research Section B: Beam Interactions with Materials and Atoms*, volume 268, pages 1818–1823, June 2010.

[36] C. Uzan-Saguy, C. Cytermann, R. Brener, V. Richter, M. Shaanan, and R. Kalish. Damage threshold for ionâĂŘbeam induced graphitization of diamond. *Applied Physics Letters*, 1995.

[37] L. Mandel and E. Wolf. Coherence properties of optical fields. *Review of Modern Physics*, 1965.

[38] Sara Mouradian, Noel H. Wan, Tim Schroder, and Dirk Englund. Rectangular photonic crystal nanobeam cavities in bulk diamond. *Applied Physics Letters*, 2017.

[39] Noel H. Wan, Sara Mouradian, and Dirk Englund. Two-dimensional photonic crystal slab nanocavities on bulk single-crystal diamond. *Applied Physics Letters*, 2018.

[40] T. Gaebel, M. Domhan, C. Wittmann, I. Popa, F. Jelezko, J. Rabeau, A. Greentree, S. Prawer, E. Trajkov, P.R. Hemmer, and J. Wrachtrup. Photochromism in single nitrogen-vacancy defect in diamond. *Applied Physics B*, 2005.

[41] N. Aslam, G. Waldherr, P. Neumann, F. Jelezko, and J. Wrachtrup. Photo-induced ionization dynamics of the nitrogen vacancy defect in diamond investigated by single-shot charge state detection. *New Journal of Physics*, 2013.

[42] S. Ditalia Tchernij, T. Luhmann, J. Forneris, T. Herzig, J. Kupper, A. Damin, S. Santonocito, P. Traina, E. Moreva, F. Celegato, S. Pezzagna, I.P. Degiovanni, M. Jaksic, M. Genovese, J. Meijer, and P. Olivero. Photoluminescence of lead-related optical centers in single-crystal diamond. *arXiv*, 2018.

[43] K. Beha, A. Batalov, N. B. Manson, R. Bratschitsch, and A. Leitenstorfer. Optimum photoluminescence excitation and recharging cycle of single nitrogen-vacancy centers in ultrapure diamond. *Physical Review Letters*, 2012.

[44] P. Siyushev, H. Pinto, M. Voros, A. Gali, F. Jelezko, and J. Wrachtrup. Optically controlled switching of the charge state of a single nitrogen-vacancy center in diamond at cryogenic temperatures. *Physical Review Letters*, 2013.

[45] U. F. S. D'Haenens-Johansson, A. M. Edmonds, B. L. Green, M. E. Newton, G. Davies, P. M. Martineau, R. U. A. Khan, and D. J. Twitchen. Optical properties of the neutral silicon split-vacancy center in diamond. *Physical Review B*, 2011.

[46] B. Machielse, S. Bogdanovic, S. Meesala, S. Gauthier, M. J. Burek, G. Joe, M. Chalupnik, Y. I. Sohn, J. Holzgrafe, R. E. Evans, C. Chia, H. Atikian, M. K. Bhaskar, D. D. Sukachev, L. Shao, S. Maity, M. D. Lukin, and M. Loncar. Electromechanical control of quantum emitters in nanophotonic devices. *arXiv*, 2019.

[47] M.-A. Lemonde, S. Meesala, A. Sipahigil, M. J. A. Schuetz, M. D. Lukin, M. Loncar, and P. Rabl. Phonon networks with siv centers in diamond waveguides. *Physical Review Letters*, 2018.

[48] A. Sipahigil, R. E. Evans, D. D. Sukachev, M. J. Burek, J. Borregaard, M. K. Bhaskar, C. T. Nguyen, J. L. Pacheco, H. A. Atikian, C. Meuwly, R. M. Camacho, F. Jelezko, E. Bielejec, H. Park, M. Loncar, and M. D. Lukin. An integrated diamond nanophotonics platform for quantum-optical networks. *Science*, 2016.

[49] R. E. Evans, M. K. Bhaskar, D. D. Sukachev, C. T. Nguyen, A. Sipahigil, M. J. Burek, B. Machielse, G. H. Zhang, A. S. Zibrov, E. Bielejec, H. Park, M. Loncar, and M. D. Lukin. Photon-mediated interactions between quantum emitters in a diamond nanocavity. *Science*, 2018.

[50] Tsung-Ju Lu, Michael Fanto, Hyeongrak Choi, Paul Thomas, Jeffrey Steidle, Sara Mouradian, Wei Kong, Di Zhu, Hyowon Moon, Karl Berggren, Jeehwan Kim, Mohammad Soltani, Stefan Preble, and Dirk Englund. Aluminum nitride integrated photonics platform for the ultraviolet to visible spectrum. *Optics Express*, 2018.

[51] Cheng Wang, Mian Zhang, Brian Stern, Michal Lipson, and Marko Loncar. Nanophotonic lithium niobate electro-optic modulators. *Optics Express*, 2018.

[52] Sara L. Mouradian, Tim Schroder, Carl B. Poitras, Luozhou Li, Jordan Goldstein, Edward H. Chen, Michael Walsh, Jaime Cardenas, Matthew L. Markham, Daniel J. Twitchen, Michal Lipson, and Dirk Englund. Scalable integration of long-lived quantum memories into a photonic circuit. *Physical Review X*, 2015.

[53] Mihir Pant, Hyeongrak Choi, Saikat Guha, and Dirk Englund. Percolation based architecture for cluster state creation using photon-mediated entanglement between atomic memories. *arXiv*, 2017.